The performance of the SPHERE sub-systems in the integration lab

Francois Wildi[1], Jean-Luc Beuzit[b], Markus Feldt[c], David Mouillet[b], Kjetil Dohlen[a], Pascal Puget[b], Andrea Baruffolo[d], Julien Charton[b], Anthony Boccaletti[e], Riccardo Claudi[d], Anne Costille[b], Philippe Feautrier[b], Thierry Fusco[g], Raffaele Gratton[d], Markus Kasper[h], Maud Langlois[k], Patrice Martinez[b], Dino Mesa[d], David Le Mignant[a], Alexey Pavlov[c], Cyril Petit[g], Johan Pragt[i], Patrick Rabou[b], Sylvain Rochat[b], Ronald Roelfsema[i], Jean-François Sauvage[g], Hans-Martin Schmid[j], Eric Stadler[b], Claire Moutou[a].

[1] Observatoire de Genève, CH-1290 Sauverny, Switzerland
[a] Laboratoire d'Astrophysique de Marseille, B.P. 8, F-13376 Marseille Cedex 12, France
[b] Laboratoire d'Astrophysique de Grenoble, B.P. 53, F-38041 Grenoble Cedex 9, France
[c] Max Planck Institut für Astronomie, Königstuhl 17, D-69117 Heidelberg, Germany
[d] Osservatorio Astronomico di Padova, Vicolo dell'Osservatorio 5, I-35122 Padova, Italy
[e] Laboratoire d'Etudes Spatiales et d'Instrumentation en Astrophysique, F-92190 Meudon, France
[f] Laboratoire Universitaire d'Astrophysique de Nice, Parc Valrose, F-06108 Nice, France
[g] Office National d'Etudes et de Recherches Aérospatiales, B.P. 72, F-92322 Chatillon, France
[h] European Southern Observatory, Karl-Schwarzschild-Strasse 2, D-85748 Garching, Germany
[i] ASTRON, P.O. Box 2, NL-7990 AA Dwingeloo, The Netherlands
[j] Institute of Astronomy, ETH Zurich, CH-8092 Zurich, Switzerland
[k] Laboratoire d'Astrophysique de Marseille, B.P. 8, F-13376 Marseille Cedex 12, France, now at CRAL

ABSTRACT

SPHERE, the extra-solar planet imager for the Very Large Telescope is a program that has been running since 2006. The instrument is now nearing completion and it is in the final integration stage. The 3 science instruments of SPHERE are now complete and have passed the internal acceptance review while the complex common path with the extreme Adaptive optics system, the coronographs and the calibration module is aggressively progressing. This paper reviews the performance of the Common Path (CP) and three science instruments of SPHERE: IRDIS, the dual band imager; IFS, the integral field spectrograph and ZIMPOL, the imaging polarimeter. We also present an outlook at the final system integration.

Keywords: exo-solar planets, extreme adaptive optics, coronagraphy, dual band imaging, polarimetry, spectral imaging

1. INTRODUCTION

The top objective of the Spectro-Polarimetric High-contrast Exoplanet Research (SPHERE) instrument for the VLT is the discovery and study of new extra-solar giant planets orbiting nearby stars by direct imaging of their circumstellar environment. The design of SPHERE is optimized towards reaching the highest contrast in a limited field of view and at short distances from the central star. Both evolved and young planetary systems will be detected, respectively through their reflected light (mostly by visible differential polarimetry) and through the intrinsic planet emission using IR differential imaging and integral field spectroscopy. The design of SPHERE and its expected performance has been the subject of prior publications [1], [2].

With a gain of two orders of magnitudes in contrast with respect to existing instruments and a list of potential targets including several hundred stars, SPHERE will provide a clear view of the frequency of giant planets in wide orbits. With the number of expected detections (several tens), the level of the large separation wing of the distribution with semi-major axis can probably be estimated with an accuracy of about 20-30%, good enough for a first statistical discussion of

[1] francois.wildi@unige.ch

the properties of planetary systems. Beside frequency, it would also be interesting to derive the distributions of planets parameters such as mass, semi-major axis and eccentricities.

Furthermore, a direct imager like SPHERE provides the only way of obtaining spectral characteristics for outer planets. The SPHERE differential polarimetric channel (ZIMPOL) might also allow detecting a few planets shining by reflecting stellar light. Such an instrument will provide invaluable information with which to hone models in preparation for the ELTs. SPHERE will be highly complementary to current and contemporaneous studies of exo-planets.

2. COMMON PATH

In terms of complexity, the Common Path is SPHERE's most demanding sub-system. It includes the main mechanical structure, transfer optics to the three science ports, visible (VIS) and near infrared (NIR) coronagraphy, a calibration modules, numerous electrical cabinets and housings, damping system, central cryogeny, central vacuum, etc.
After separate integration the main optical bench has been installed on the instrument baseframe which provides both active pneumatic damping and a physical support allowing sliding away from the telescope focus for maintenance. Everything but some electrical cabinets is now hidden from the view in a laminar flow enclosure obscured with black curtains until the final thermal/dust enclosure is finished.
Most of the optical path is populated now with the final components, with the exception of 2 mirrors which are (re)manufactured and with dummy mirrors instead of the adaptive optics components, tested on a separate bench. Optical interfaces to the science instruments have been verified with both wavefront error and transmission in spec at all the ports:

Mode	Static wavefront error from VLT Nasmyth focus	
Main survey mode , 950-1350 to IFS, H-band to IRDIS	<67nm to IRDIS	<69nm to IFS
Extended IFS mode, 950-1700 to IFS, Ks to IRDIS	<69nm to IRDIS	<69nm to IFS
IRDIS only	<68nm to IRDIS	
All NIR science modes (100% VIS on WFS)		< 65 nm to WFS
ZIMPOL broad band	<65nm to ZIMPOL	<65nm to WFS
ZIMPOL R-band	<65nm to ZIMPOL	<95nm to WFS

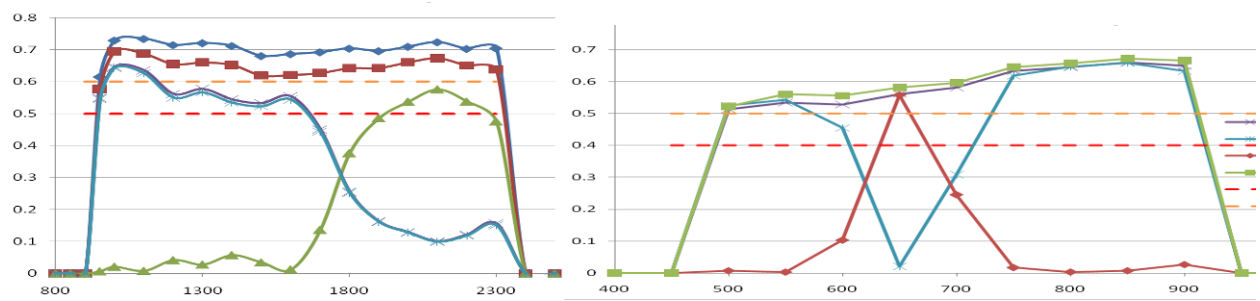

Figure 1. Transmission of the SPHERE Common Path. NIR path on the left, VIS path is on the right. NIR: the red squares curves represent the transmission in "IRDIS alone" mode. The blue crosses is the transmission to the IFS and the green triangles the transmission to IRDIS, both in the NIR survey mode. VIS: The purple crosses represent the transmission to the wave front sensor for NIR science. The blue crosses represent to transmission to the WFS when observing in R-band with ZIMPOL. The red diamonds are the R-band transmission to ZIMPOL

The coronagraphs have been co-aligned on the NIR and VIS coronagraph wheels, and the wheels have been aligned on the CP bench. The apodizer wheel is not yet available on CPI, thus the Apodized Pupil Lyot Coronagraph cannot be tested. The achromatized four-quadrant phase mask performance is given below; one of the most promising coronagraphs. Figure 2 shows the PSF at 1.55 µm with Strehl ratio (SR) estimated to be 93 ± 2 %. The SR was determined by measuring the peaks intensity ratio of the experimental PSF to that of the theoretical PSF normalized to the total intensity.
Measured performance (peak rejection and contrast curve) is in fair agreement with performance obtained during coronagraphs lab tests . Measurements have been done with a laser source at 1.55um in the VLT pupil configuration. Better performance can potentially still be obtained with slight tuning of component alignment.

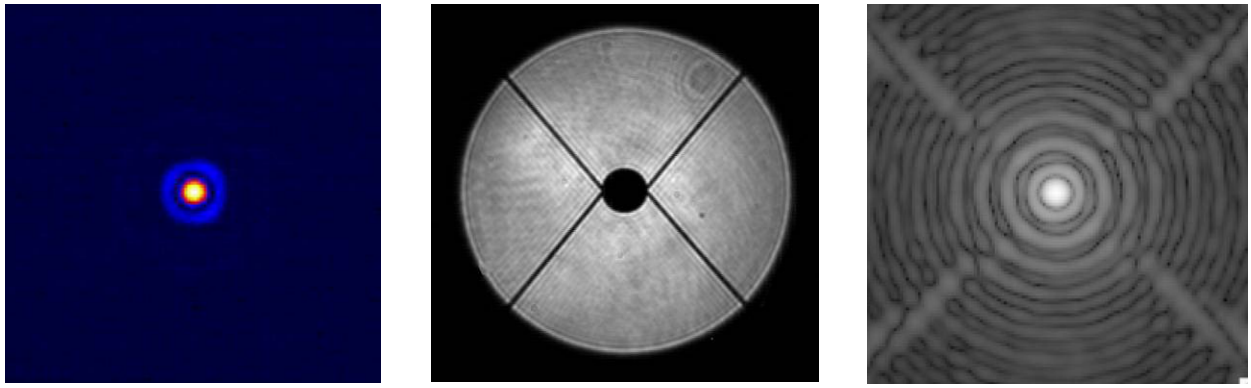

Figure 2. Left: measured IR PSF at 1.55 um, SR ~93%, middle: VLT pupil image recorded, right: reconstructed PSF from VLT pupil recorded to generate theoretical PSF for SR ratio estimation.

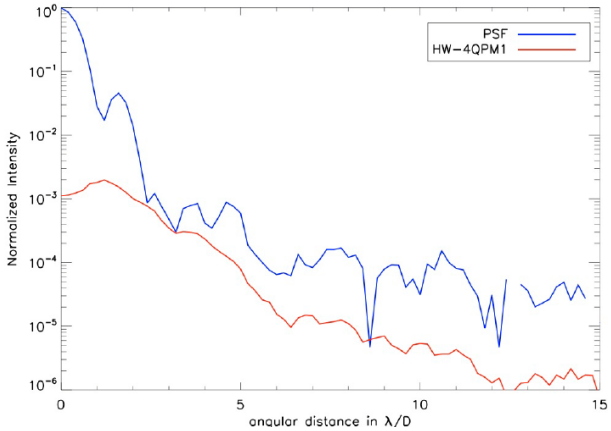

Figure 3.Four quadrant phase mask coronagraph #1 contrast curves at 1.55um (laser light) Raw performance estimation:

- Total rejection = 145
- Peak rejection = 505 (600 H-band R=7 measured on coronagraphic test bench)
- Contrast at = 3.4 10^{-4} @ 3λ/D, 7.9 10^{-5} @ 5λ/D, 5.4 10^{-6} @ 10λ/D and 1.3 10^{-6} @ 12λ/D

3. ADAPTIVE OPTICS

The design of the adaptive optics (AO) system of SPHERE has been presented earlier in [3] and this system has been in integration for some time now [4]. It is integrated in a separate facility and will be put on the common path after it is fully validated. All main AO components are now present:

Component	Component Status + functionality status
High Order Deformable Mirror: CILAS 41x41 piezo stack DM	Model #1, limitations: flatness, 4 dead actuators, and high frequency behavior
Image Tip Tilt Mirror, high speed tip-tilt	OK, functional up to 125Hz because of WFS
Differential Tip Tilt Plate, to correct the tip-tilt between wavefront sensor (WFS) visible beam and NIR beam	OK, differential TT loop OK at nominal speed (between 1 and 10 Hz)
Pupil Tip Tilt Mirror, to keep the pupil location stable in SPHERE	OK, pupil loop OK at nominal speed
40x40 Shack-Hartmann WFS,	Prototype, see below, limited to 125 Hz
Spatial filter (variable square pinhole)	OK, spatial filtering functionality OK
NIR Differential Tip-Tilt Sensor	OK, differential TT loop OK
Real Time Controller	Software version 5, all loops OK to max speed, control laws OK, some high level functionalities

Presently the functions of the real time controller (RTC) are being systematically verified. The main loop has been closed if only at 125Hz, because the WFS data needs to be reformatted in real time to conform to the RTC format. Experimental rejection transfer functions have proved to be consistent with theory. Auxiliary control loops, for pupil stabilization and differential Tip-Tilt compensation have also been closed simultaneously, though characterization and optimization of these loops are still pending. The use of the spatial filter has been verified in an unexpected way: One of the AO test bench optics is diamond turned and produces multiple images of the guide star by diffraction. When the spatial filter is opened too much, these images create aliases on the Shack-Hartmann sensor and degrade the image quality. See the figure below. Reduction of the filter size leads to complete suppression of these aliased components and image quality improvement.

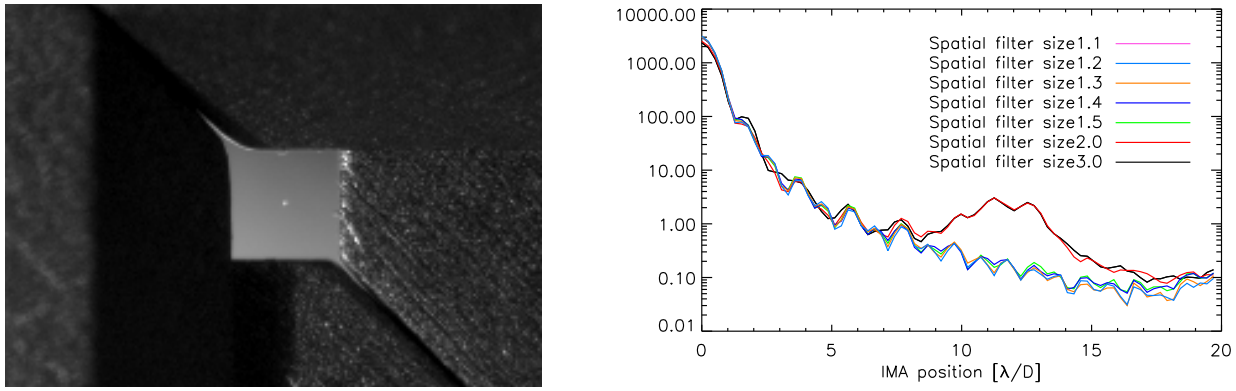

Figure 4.Four. The spatial filter of the AO system. The picture on the left shows the spatial filter and the guide star in the middle. The R/h curve shows how the spatial filter cut's off the aliases created by higher frequency components (size of spatial filter in λ/d).

The correction of the non-common path aberrations (NCPA) has also been demonstrated. The NCPA are one of the main limitations of any AO system. These static aberrations are introduced after beam splitter and all the way down to the imaging camera. They are unseen by the wave-front sensor and therefore not compensated by closed AO loop. The method implemented to compensate for these NCPA is to measure them in the imaging focal plane (here the IR DTTS) and to modify the reference slopes of the AO system to perform the compensation. The Figure 5 shows the result of the pre-compensation method implemented at SAXO-MEUDON, which is fully compliant with the expected performance. This procedure has also been validated in the coronagraphic focal plane.

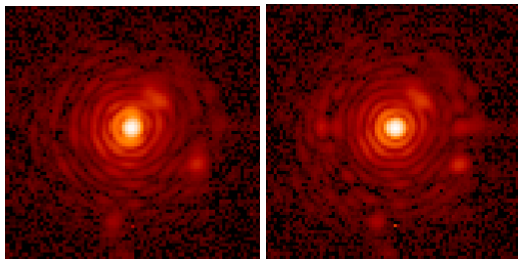

Figure 5. Closed loop PSF on DTTS IR sensor. The source is at bench entrance. No artificial turbulence added. [Left] before NCPA compensation. [Right] after NCPA compensation. 220 Zernike modes have been compensated. The compensation effect is clearly visible up to the 5th Airy rings. Three ghosts are clearly visible, due to parasitic reflections on DTTS entrance window (top right) and due to unoptimized neutral filters(bottom right and left).

4. IRDIS THE NIR DUAL BAND IMAGER AND SPECTROGRAPH

4.1 IRDIS description and science requirements

IRDIS provides simultaneous imaging in two color bands which we call dual band imaging (DBI). It has a spectral range of 950-2320 nm and an image scale of 12.25mas/pixel consistent with Nyquist sampling at 950nm. The FOV is 11"x12.5" in classical imaging and Ø11" in DBI. A beam splitter plate associated with a mirror separates the beam in two parallel beams, focalized side-by-side onto a common detector. Before reaching the detector, the beams are spectrally filtered by dual band filters (DBF) with adjacent pass-bands corresponding to sharp features in the expected

planetary spectra.[5] Differential aberrations between the two beams are critical for the performance of differential imaging of extrasolar planets[6].
IRDIS DBI mode will allow the use of different data analysis methods to remove the speckle residuals, in particular simultaneous Spectral Differential Imaging (SDI), for which the main limitation are the quasi-static aberrations upstream the coronagraph and the spectral separation between the DBI filters, and Angular Differential Imaging (ADI) which uses the fact that the observations are obtained in pupil-tracking mode, and for which the main limitations are the field rotation rate and the temporal evolution of the aberration. IRDIS also has a Long Slit Spectroscopy (LSS) mode, which, combined with an efficient data analysis method,[8] offers the possibility of spectral characterization of detected objects at low resolution (LRS, R = 60) and medium resolution (MRS, R = 420). A dual polarimetric imaging mode provides simultaneous imaging in two orthogonal polarizations within any of the broad and narrow-band filters. IRDIS used alone in its various modes will allow obtaining observations in all bands from Y to short-K, either in dual imaging or in classical imaging with broad and narrow-band filters. This will be especially interesting in order to characterize already detected and relatively bright targets. Additional science cases will also benefit from these observing modes (disks, brown dwarfs, etc.).

Table 1. Summary of IRDIS observing modes and main characteristics.

Mode	Use Science case	Wavelength Bands	Rotator mode	Filters, Resolution	Contrast Performance (1h, SNR=5, H<6)
Dual Band Imaging	Survey mode (H only) Characterization of cool outer companions	Y,J,H,Ks	Pupil or field stabilized	6 pairs R=20-30	~ 10^{-5} at 0.1” ~10^{-6} at 0.5”
Dual Polarimetry Imaging	Reflected light on extended environment	Y,J,H,Ks	Pupil or field stabilized	4 Broad 10 Narrow bands	~ 10^{-4} at 0.1” ~ 10^{-5} at 0.5” 30% circumstellar source
Slit Spectroscopy	Characterization of not too faint companions	LRS : Y-Ks MRS: Y-H	Pupil stabilized	LRS : R=60 MRS : R=420	~ 3.10^{-4} at 0.3” ~ 10^{-5} at 0.5”
Classical Imaging	Environment with no spectral features	Y,J,H,Ks	Pupil or field stabilized	4 Broad 10 Narrow bands	~ 10^{-3} at 0.1” ~ 3.10^{-4} at 0.5

4.2 IRDIS architecture

The opto-mechanical design of IRDIS is shown in Figure 6 (left). The IRDIS entrance pupil is the coronagraphic exit pupil (Lyot stop). Located in a collimated beam of diameter 10mm, it constitutes the main optical interface parameter with the common path optics. Three wheels are provided within the cryogenic environment: the common filter wheel carrying classical imaging filters, the Lyot stop wheel, and the dual imaging filter wheel. The detector is mounted on a two axis piezo motor translation stage to allow dithering for flat-field improvement. The cryostat interior is shown in Figure 6 (right). The optical bench with its cold screen is thermally strapped to a small, cylindrical LN2 tank, constantly maintained full by the large LN2 tank on the side.

4.3 IRDIS AIT

As of June 2011, we have assembled the cryostat and checked its cryo-vacuum performances. The filter wheels are assembled and tested and all IRDIS optics have been integrated inside the cryostat (except the polarizers and few filters) and tested. Functional tests, detector alignment, final optical performance verification and science performance characterization with the science-grade detector have been performed. This preliminary testing phase has allowed to validate the functionality and performance of IRDIS alone in terms of instrument control and data processing capabilities, as well as calibration and operational strategies.

4.3.1 Imaging properties

Phase diversity analyses have been performed to evaluate the aberrations in the two channels. The analysis was done on a set of 60 Zernike coefficients. The total common path wavefront error is 16nm rms, well within the spec, and in good agreement with measurements obtained interferometrically. The DBI-mode differential wavefront error is 6.4nm rms, well within the spec (10nm rms) and very close to the 5nm rms goal. This level of differential aberration is compatible with 5-sigma contrast of 10^{-5} to 10^{-6} from 0.1” to 0.5’’.

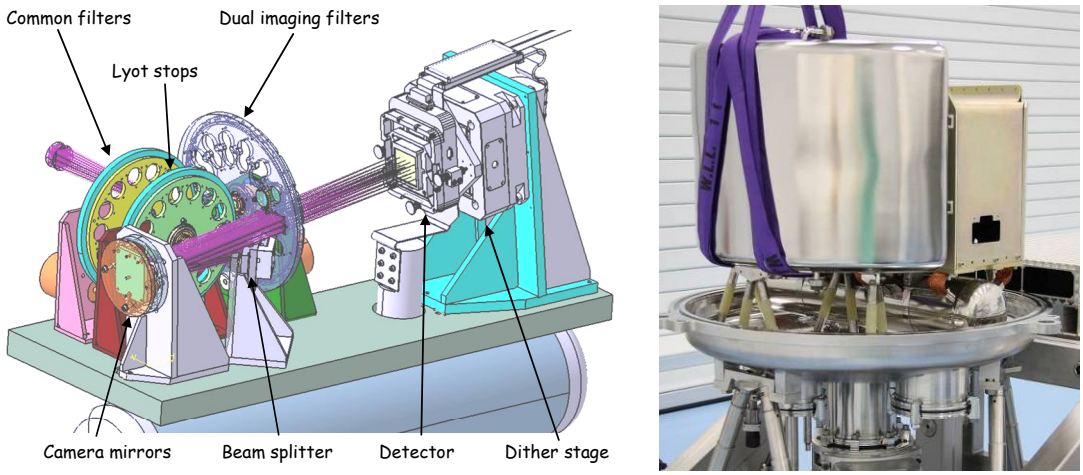

Figure 6. IRDIS opto-mechanical implementation (L/h) and the interior of the cryostat during integration (R/h).

4.3.2 Detector properties

The detector is a 2Kx2K Hawaii-2RG array operated in 32-channel read-out mode by the ESO new generation controller. Excellent read noise as low as 8.3 electrons for double correlated sampling and down to 4.6 electrons for Fowler sampling has been confirmed at the operation temperature of 80 K. Correlated noise exists and has a non-negligible impact on the final readout noise, but since its level strongly depends on the environment of the experiment, its impact can only be properly quantified at the telescope.

Bias level tuning has brought the electrical cross-talk level down from 1% to about 0.05%. Non-linearity within a few percent, compatible with science requirements, is achieved up to 25000ADU. While the conversion gain remains to be precisely established, an estimated gain of 2.0 e-/ADU therefore indicates a dynamic range of 50000e-. Somewhat lower than expected, efficiency analysis shows this to be tolerable since mainly bright targets will be affected.

An important limitation in high contrast imaging with IRDIS is the accuracy of flat fielding. Measurements show that 90 second flat field integration was sufficient to be dominated by pixel-to-pixel sensitivity variations and not by the photon noise of the flat field exposure. We measured the following rms values:

- Typical value for the PRNU over areas of 100x100 pixels: 0.036
- Typical flat field accuracy obtained by simple division with a flat field image: 3.8×10^{-3}
- Typical flat field accuracy obtained by using a 10x10 dithering procedure: 2×10^{-3}.

Persistence has been evaluated by observing the apparent flux level following detector saturation. A level of 0.1% of the reference flux is reached after about 90s.

4.3.3 Scientific performance

The performances in dual band imaging were evaluated by reducing long exposure data with singular differential imaging and double differential imaging. After classical prereduction of the data, the images were shifted in translation and a zoom (lambdaH2/lambdaH3) was applied before the final image subtraction (Single difference image: SDI). The double difference (DD) image was obtained by combining the two sets of SD images taken in H23 and H32. The 1-sigma contrast reaches 4.10^{-5} at large separation and (DD) 10^{-3} close to the PSF center. Assuming that the PSF subtraction efficiency will similar when using a coronograph, we expect that there will be an increase in contrast by a factor 10-100 with a coronograph and as a consequence this level of performance is compatible with the expected performances. We already clearly see the high efficiency of the PSF subtraction, which depends on the similarity of aberrations between the two quadrants and is corroborating the very good optical quality of IRDIS.

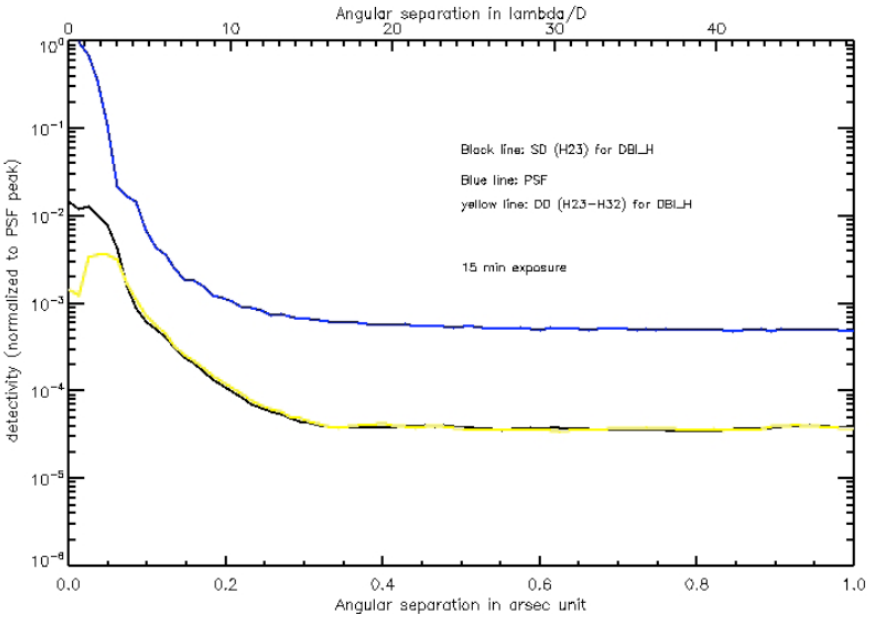

Figure 7. IRDIS radial profile of the 1 sigma detectivity normalized to the PSF maximum in DBI-H

5. IFS THE INTEGRAL FIELD SPECTROGRAPH

The IFS[9] will allow imaging of giants gaseous planets around young (<100 Myr) and nearby (<100 pc) stars. It can be configured to work between 0.95 and 1.35 μm with a resolution of 50 or 0.95 - 1.65 μm with a resolution of 30. It will have an approximately square field of view with a side of 1.77 arcsec. The integral field unit (BIGRE) is a lenslet array sampling the focal plane with a pitch of 161.5 μm, corresponding to 12.25 mas projected on space; in total about 21000 spaxels are obtained. In the BIGRE concept[10], each lenslet is an afocal system made of two lenses (i.e. active surfaces on both faces of the array), which produces an array of virtual slits each one corresponding to a portion of the focal plane, with a suitable demagnification factor. Since each lenslet samples much less than a diffraction peak, the whole system is diffraction limited. The remaining part of the IFS is a traditional spectrograph composed of a collimator, a camera and a low resolution disperser (Amici prism), producing an array of short (~39 pixels long) spectra on a Hawaii II 2kx2k detector. After appropriate calibrations and reduction, a datacube composed of 39 monochromatic images is obtained. Most of the instrument is warm: only the detector and a cold filter are within a LN2 dewar. Appropriate baffling ensures a low thermal background (<10 e-/s/pixel).

The images of the datacube can be appropriately combined using various differential imaging methods (e.g. Simultaneous Spectral Differential Imaging or Spectral Deconvolution[11]) with the aim to subtract the speckle noise from the star and to make emerge the signal from eventual companion objects. In the last years simulations were performed to test the instrument performances and proved the capability of the instrument to get down to luminosity contrast of the order of a few 10^{-7} with respect to the host star at a separation of some tenth of arcsec[12].

The IFS is now complete at the Padova Astronomical Observatory (see Figure 8). Functional and performance tests were run and the data produced was used to test and tune its Data Reduction and Handling (DRH) software. All these tests have been performed using a simulator of the SPHERE Common Path, but without the extreme AO system and coronagraphs. Complete tests will be run later when the IFS is integrated with the rest of SPHERE.

Tests included verification of the IFS geometry, focusing and optical quality, transmission, thermal background, cross talk, and accuracy of flat fielding. All these tests were passed successfully, the IFS being within or very close to the technical specifications.

In particular a full test comprising all the calibrations and an observation of a simulated star has been performed. An enlargement of the central part of the image as read on the detector is shown in the left panel of Figure 9, in order to make visible the spectra given by individual lenslets. This image is the median of 80 2-sec images obtained by illuminating the BIGRE with a continuum lamp, and inserting a 0.4 mm diaphragm within our simulator of the CP some 140 mm in front of the BIGRE. The beam provided by the CP simulator is collimated and on the BIGRE there is then a

diffraction image, roughly an Airy pattern which first diffraction ring is quite clearly visible. Note that the Strehl ratio of this image is very high (0.99) due to the good optical quality of the CP simulator. The original image was dithered 4x4, with 5 images obtained at each dithering location; the image was de-dithered before doing the median. Applying dithering allows to virtually eliminating hot pixels from the median image, so that this image appears very clean.

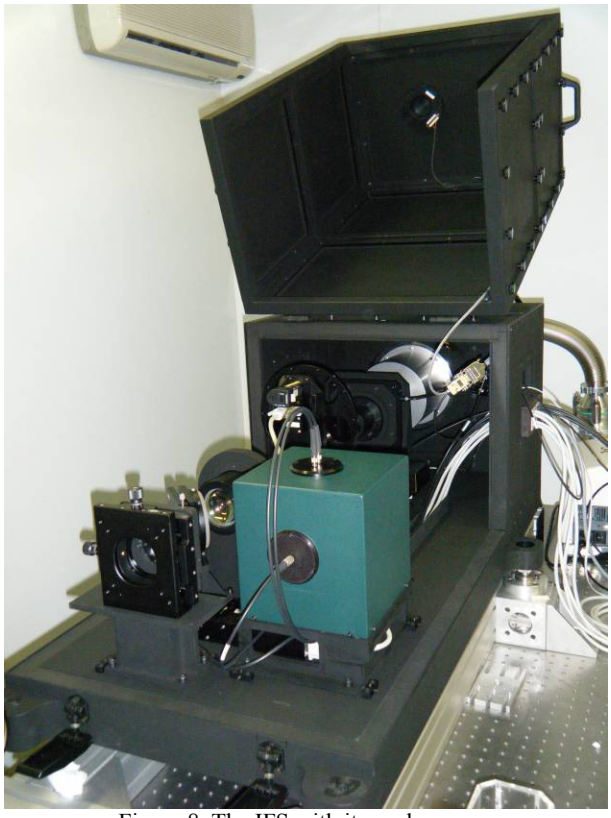

Figure 8. The IFS with its enclosure open.

The image on the right panel of Figure 9 is the result of our analysis of this series of images (a total observing time of 160 sec). We used the DRH recipes to subtract dark, flat field the image, extract the spectra provided by individual lenslet, wavelength calibrate them and transform the image into a datacube with square spatial sampling and constant wavelength step. We then applied the spectral deconvolution method of Thatte et al.[3] to subtract speckles (which are however almost negligible due to the very high Strehl of the image). Since residuals are obtained in this way, the central peak is much reduced. Finally, we collapsed the datacube in a single image by cross correlating each spectrum with a template (actually, the spectrum of an M star from our library). The gray scale of this image is in e-; note that before application of the spectrum deconvolution, peak intensity of the image on the datacube was ~10^4 e-, so that the grey scale roughly goes from -5x10^{-5} to 5x10^{-5} of the peak intensity. In fact, the 5-sigma contrast that we can derive from this image is ~3x10^{-5} at separations >0.3 arcsec, and agrees with the expected noise level for this image (see Figure 10). The dominant source of noise in this case is detector read out noise; this is because our setup simulates a (non-coronagraphic) observation of a very faint source (J=9.5).

In such a case, optimization of the observation would have required longer DIT's: however, we wished to avoid saturation in the central peak of the image, and we then kept DITs of 2 sec. With a coronagraph attenuating by a factor of some 100 the central peak, much longer DIT's would have been possible, achieving a better 5-sigma contrast.

This image has been obtained using the optimized setting for the detector, which minimizes the electric cross talk. Even so, a faint "electric ghost" is still visible on the left of the image, with intensity ~10^{-4} of the peak value.

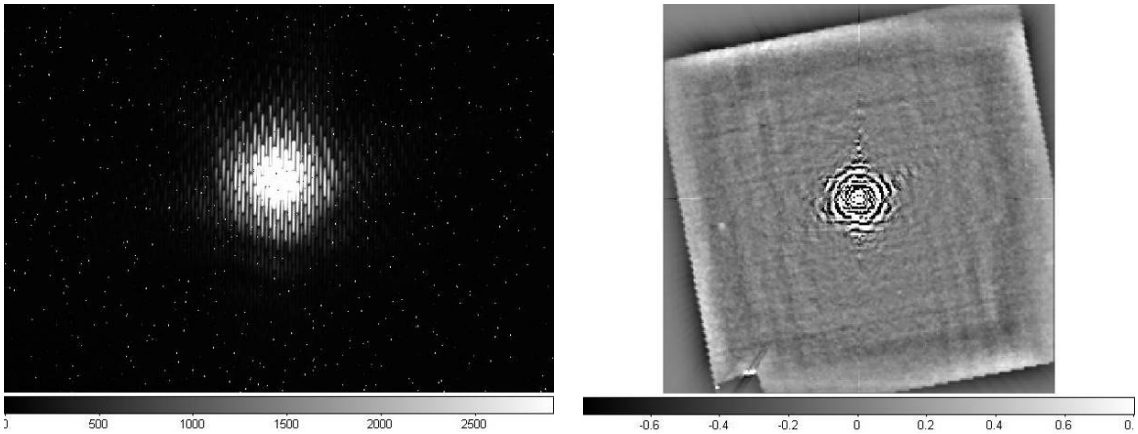

Figure 9. Left panel: enlargement of the central part of an image resulting from the simulation of a scientific observation of a J=9.5 star. Right panel: final image resulting from the data reduction of the left image using the DRH recipes and a dedicated IDL routine.

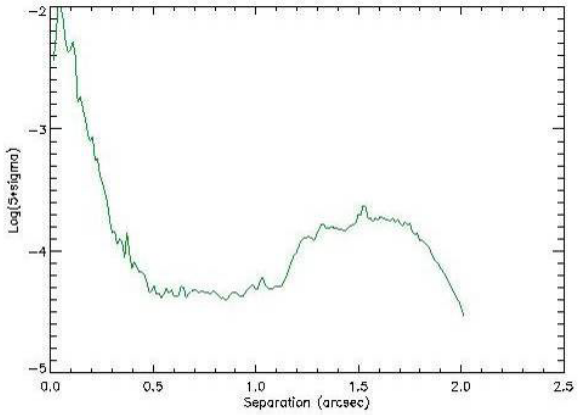

Figure 10. A contrast of the order of 4.5×10^{-4} is obtained at a separation of 0.5 arcsec. This has been obtained for an instrumental setup without any coronagraph and using a very simple simulation of the SPHERE Common Path.

6. ZIMPOL THE HIGH RESOLUTION POLARIMETER

6.1 ZIMPOL science case

ZIMPOL[14],[15],[16] (Zurich Imaging Polarimeter) is one of the first instruments which aim for the direct detection of reflected light from extra-solar planets. It will search for direct light from old planets with orbital periods of several months to several years as we know them from our solar system. The reflected radiation is generally polarized and the degree of polarization may be particularly high at short wavelengths < 1μm due to Rayleigh scattering by molecules and by haze particles in planetary atmospheres[17],[18]. For a Jupiter-sized object and a separation of 1 AU the planet/star contrast to be achieved is on the order of 10^{-8} for a successful detection. This is much more demanding than the direct imaging of young self-luminous planets.

6.2 ZIMPOL architecture

The optical train (Figure 11) contains a common optical path that is split in two arms by a polarizing beamsplitter. The common path contains common components for both arms like calibration components, common filters, a switchable half wave plate and a Ferro Electric Liquid (FLC) crystal polarization modulator. The two arms measure simultaneously the two complementary polarization states in the same or in distinct filters. Each arm has its own detector and they are both located in the same cryostat and cooled to -80 ^{o}C. The rest of the ZIMPOL opto-mechanical system is at ambient.

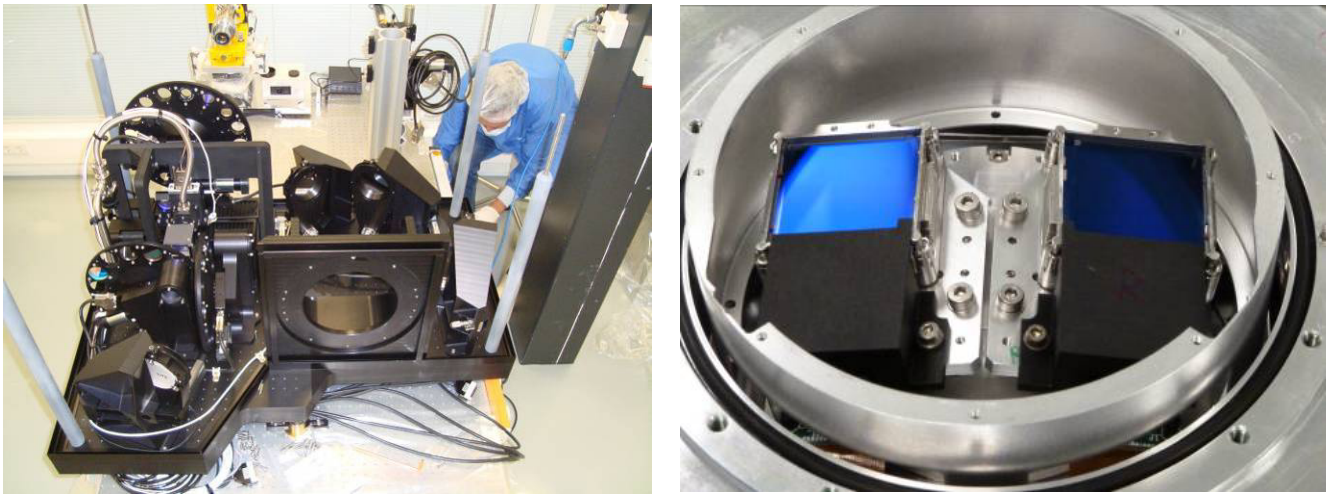

Figure 11. The ZIMPOL bench during integration (L/h). ZIMPOL CCDs S1 and S2 mounted and aligned in the cryostat (R/h)

ZIMPOL uses two e2v frame transfer CCD44-82 2Kx4K Std Silicon CCDs located in a modified ESO Double Detector Head and Continuous Flow Cryostat. They are read-out binned 2x2 by one ESO New Generation Controller.

Both CCD's are very clean and have only of the order ~20 low (~50% or less) efficiency pixels / pixel pairs. There are another ~20 with less reduced efficiency (~60-80%). An extensive bias stability measurement was made and showed a maximum excursion of 6 counts for CCD1 and 3 counts for CCD2 on an overall level of about 1000 counts. We consider this bias stability as excellent. The dark current is 0.2 e-/pix/s for fast and window polarimetry and less than 0.04 e-/pix/s for the other modes. Preliminary measurements of the overall modulation / demodulation efficiency of ZIMPOL were carried out. For fast polarimetry the measured efficiency was 82% for arm 1 and 77% for arm 2. These values are within the specification of 75% but miss the fast polarimetry goal of 90% quite a bit.

6.3 PSF Quality

The PSF quality and the Strehl ratio for all ZIMPOL filters have been verified. For the ZIMPOL pre-optics we have measured a WFE of about λ/20 (633 nm). For ZIMPOL we have calculated a WFE of about λ/17 (excluding filters) and for one filter we assume a WFE of λ/20. Figure 12 shows the measured and calculated Strehl values based on the numbers given above. From the plot we can conclude that apparently the RMS WFE is slightly better than expected.

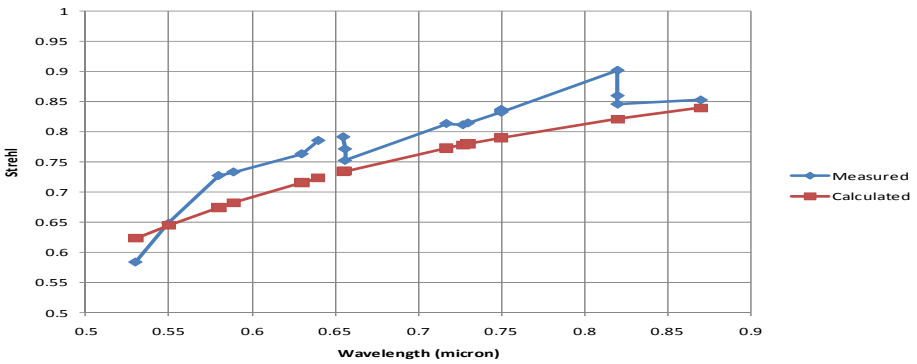

Figure 12. ZIMPOL measured and calculated Strehl Ratio for all filters.

6.4 Noise Performance

The standard deviation was calculated on some parts of the polarization images and compared to the theoretical limiting noise level calculated from the numbers of detected photons ($\sigma_p = N_{photon}^{-0.5}$). A high background polarization often has a negative impact on the small scale noise performance of a ZIMPOL type polarimeter.
Figure 13 shows the measured small scale noise level as function of detected photons for four different background polarizations and the measurement without modulator. The measurement without modulator shows that the detector system is photon noise limited already in single difference down to at least $4x10^{-6}$. A background polarization up to 1% has no significant impact on small scale noise in single and double difference.
With modulated light and measurements in single difference the noise performance is limited to about 10^{-4} due to several effects caused by the FLC modulator and the optical quality of some components close to a focal plane. Measurements with double difference remove most of the disturbing effects of single difference. The small scale noise is then photon noise limited down to about 10^{-5}.

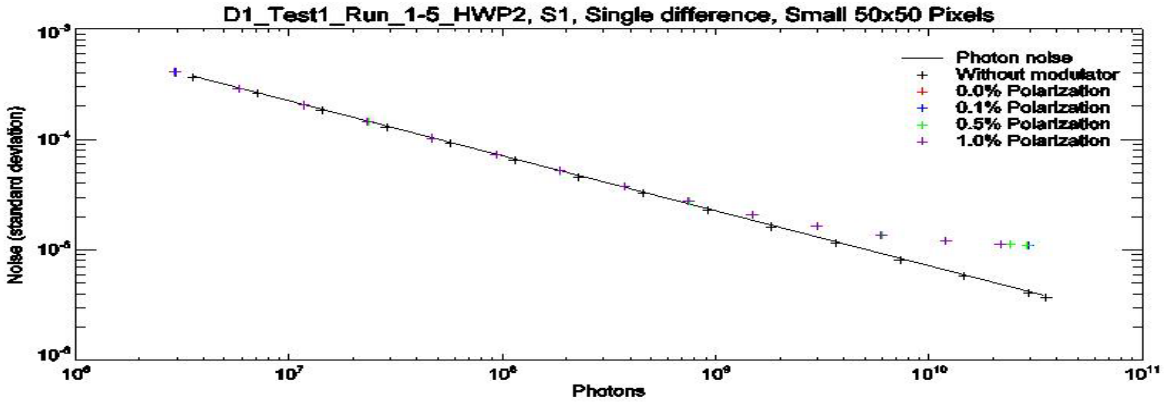

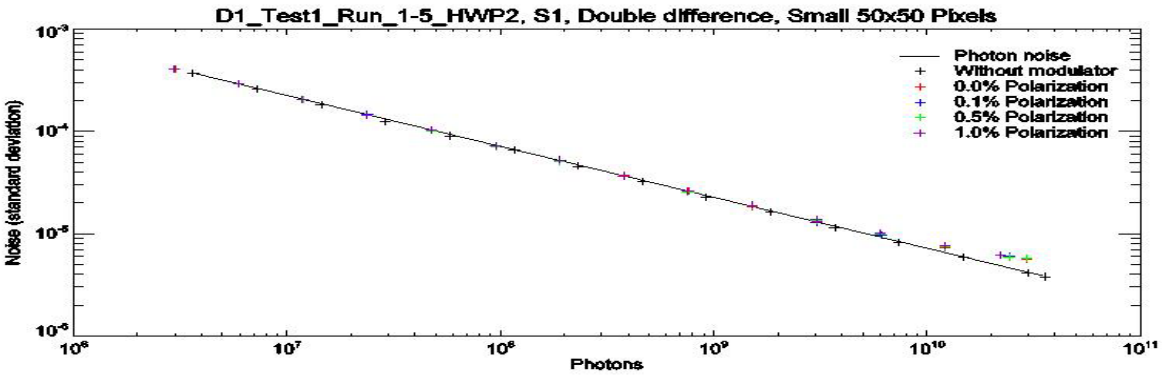

Figure 13. Noise as function of number of photons for various levels of background polarization. The straight line indicates the photon noise limit. (Top) Single Difference (Bottom) Double Difference.

6.5 High Contrast Imaging

Simulating the detection of an exoplanet in the lab requires a small polarized signal close to an unpolarized bright point source. For this purpose a fiber-based star-planet simulator has been build. The star polarization is of order 10^{-3} and the typical planet polarization is about 0.2. For high contrast measurements the intensity of the planets is reduced by ND filters and the star flux is attenuated by a coronagraph. For the measurements as presented here we have used a 3 λ/D Lyot coronagraph on a substrate. A typical result can be seen in Figure 14.

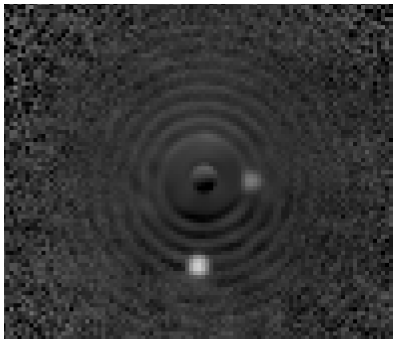

Figure 14. Double Difference high contrast image of very weak planets imaged very close to a very bright star. The planet at the right is at 80 mas from the star. The ring pattern that dominates the background noise can be clearly seen.

The intensity contrast of the planet on the right is 10^{-6} and it is detected with a 25-sigma level. So in principle we could have detected a 5 times weaker signal still with a 5-sigma level. Therefore we conclude that we can reach a 5-sigma contrast of $(10^{-6})/5 = 2x10^{-7}$ at 80 mas. Clearly we do not reach the expected overall 10^{-8} level yet.

It seems that we are mainly limited by the central star, i.e. diffraction rings that show up in polarization as a spatially modulated pattern around the PSF core and thereby it becomes the major noise source.

In the design phase we have anticipated a differential tilt effect of the FLC that shows up as a differential shift in the image plane. The HWP2 double difference technique was intended to calibrate this effect, i.e. by subtracting images taken with HPW2 at a zero position and a 45 degree rotated position the FLC effects should be removed.

However, test images as shown in Figure 14 show polarized residuals of the coronagraph diffraction rings that do not subtract in single difference and also not in double difference. We have further looked into the issue and we see that the ring pattern is caused by differential shifts. There seem to be three contributions to the differential shifts: detector offsets, FLC differential tilt and (still under debate) either HWP2 birefringence or fiber effects. Activities in the next few months will be focused on a better understanding of the observed differential beam shifts and on strategies to correct for the differential shifts in the software before combining the sub images in order to improve the contrast.

7. PROJECT STATUS

2011 is a crucial and exciting year for the project with the three science instruments undergoing full validation with static wavefront and the start of the system-level integration. The Common Path and Infrastructure sub-system is progressing fast but the completion and validation of its numerous modules is proving to be an organizational and manpower challenge. The option of integrating the adaptive optics on a separate bench was a key decision because it allows the integration, alignment and validation of all others elements to progress in parallel with the AO and will reduce strongly the time allocated to characterizing it on the final system.

The science instruments will be integrated at the pace of about one per month at the final site in Grenoble (France) starting in October. This phase includes validating the instrument software that controls the configuration of SPHERE and controls the calibration and observation sequences, as well as honing the data handling and reduction pipeline. Adaptive optics will come at the end of 2011 and will only be commissioned in early 2012. After that the final test and verification will take place with the full chain from artificial stars with phase screens generated turbulence to the science detectors through AO and coronagraphs.
The performance shown by all sub-systems is compatible with the final performance budget of SPHERE with the exception of the contrast of ZIMPOL where the point source sensitivity is currently limited by differential beam shifts.

REFERENCES

[1] K. Dohlen, J.-L. Beuzit, M. Feldt, D. Mouillet, P. Puget, F. Wildi, et al., "SPHERE: A planet finder instrument for the VLT," in: Ground-based and Airborne Instrumentation for Astronomy. McLean, Ian S.; Iye, Masanori. Eds., Proc. SPIE, Volume 6269, pp. 62-69 (2006).

[2] F. Wildi, J.-L. Beuzit, M. Feldt, D. Mouillet, K. Dohlen, P. Puget, A. Baruffolo, J. Charton, P. Baudoz, A. Boccaletti, L. Abe, R. Claudi, Ph. Feautrier, T. Fusco, R. Gratton, N. Hubin, M. Kasper, M. Langlois, R. Lenzen, A. Pavlov, C. Petit, J. Pragt, P. Rabou, R. Roelfsema, H.-M. Schmid. "SPHERE: The VLT exo-planet imager in the post-FDR phase", *Techniques and Instrumentation for Detection of Exoplanets IV*, SPIE 7440-24 (2009).

[3] T. Fusco, C. Petit, G. Rousset, K. Dohlen, J. Charton, P. Rabou, P. Feautrier, P. Baudoz, J.-L. Beuzit, D .Mouillet, P. Puget, M. Kasper, M. Downing, E. Fedrigo, N. Hubin, F. Wildi. "Design of the extrem AO system for SPHERE, the planet-finder instrument of the VLT " in Advances in Adaptive Optics II, SPIE (2006)

[4] J.-F. Sauvage, C. Petit, T. Fusco, T. Buey, A. Sevin, P. Bernardi, J. Charton, P. Feautrier, F. Wildi, K. Dohlen, J.-L. Beuzit. "First laboratory results of the SPHERE eXtreme AO system: SAXO ", SPIE 7736-14 (2010), San Diego

[5] Racine, R., Walker, G. A. H., Nadeau, D., Doyon, R., & Marois, C., "Speckle Noise and the Detection of Faint Companions," PASP, 111, 587 (1999).

[6] Cavarroc, C.; Boccaletti, A.; Baudoz, P.; Fusco, T.; Rouan, D., "Fundamental limitations on Earth-like planet detection with extremely large telescopes," Astron. Astrophys. 447, (2006), pp.397-403.

[7] Vigan, A.; Moutou, C.; Langlois, M.; Allard, F.; Boccaletti, A.; Carbillet, M.; Mouillet, D.; Smith, I., "Photometric characterization of exoplanets using angular and spectral differential imaging", MNRAS 924 (2010).

[8] Vigan, A.; Langlois, M.; Moutou, C.; Dohlen, K, "Exoplanet characterization with long slit spectroscopy", A&A 489, 1345 (2008).

[9] Claudi, R.U., Turatto, M., Giro, E. et al. "SPHERE IFS: the spectr differential imager of the VLT for exoplanet search", Proc. SPIE, 7735, 11 (2010)

[10] Antichi, J., Dohlen, K., Gratton, R. et al. "BIGRE: A Low Cross-Talk Integral Field Unit Tailored for Extrasolar Planets Imaging Spectroscopy", ApJ, 695, 1042-1057 (2009)

[11] Thatte, N., Abuter, R., Tecza, M. et al. "Very high contrast integral field spectroscopy of AB Doradus C: 9-mag contrast at 0.2 arcsec withour a coronagraph using spectral deconvolution", MNRAS, 378, 1229-1236 (2007)

[12] Mesa, D., Gratton, R., Berton, A. et al. 2011 "Simulation of planet detection with the SPHERE intergal field spectrograph", A&A, 529, 131 (2011)

[13] Claudi, R., Giro, E., Anselmi, U. et al. "Optical Design and Test of the BIGRE Based IFS of SPHERE, Proc. SPIE 8167, 67 (2011)

[14] Schmid H. M., Beuzit J.-L., Feldt M., Gisler D., Gratton R., Henning T., Joos F., Kasper M., Lenzen R., Mouillet D., Moutou C., Quirrenbach A., Stam D. M., Thalmann C., Tinbergen J., Verinaud C., Waters R., Wolstencroft R., "Search and investigation of extra-solar planets with polarimetry," IAU Colloq. 200, 165–170 (2006)

[15] D. Gisler, H.M. Schmid, C. Thalmann, H.P. Povel, J.O. Stenflo, F. Joos, M. Feldt, R. Lenzen, J. Tinbergen, R. Gratton, R. Stuik, D.M. Stam, W. Brandner, S. Hippler, M. Turatto, R. Neuhäuser, C. Dominik, A. Hatzes, Th. Henning, J. Lima, et al., CHEOPS/ZIMPOL: a VLT instrument study for the polarimetric search of scattered light from extrasolar planets. in: ``Ground-based instrumentation for astronomy", SPIE Conf. Vol. 5492, 463-474 2004

[16] Roelfsema R., Schmid, H.M. Pragt, J., Gisler D., Waters R., Bazzon A., Wildi, F et al, "The ZIMPOL high-contrast imaging polarimeter for SPHERE: design, manufacturing, and testing ," Proc. SPIE 7735-154 (2010)

[17] D. M. Stam, Spectropolarimetric signatures of Earth-like extrasolar planets, A&A 482, 989-1007 (2008)

[18] E. Buenzli, H.M. Schmid: A grid of polarization models for Rayleigh scattering planetary atmospheres, Astron. Astrophys. 504, 259-276, 2009